New Insights on Cavitating Flows Over a Microscale Backward-Facing Step

Mohammadamin Maleki[1,2], Farzad Rokhsar talabazar[1,2], Erçil Toyran[1,2], Abhinav Priyadarshi[3], Araz Sheibani Aghdam[1,2], Luis Guillermo Villanueva[4], Dmitry Grishenkov[5], Iakovos Tzanakis[3,6*], Ali Koşar[1,2,7*], Morteza Ghorbani[1,2,3,7*]

[1]Faculty of Engineering and Natural Science, Sabanci University, 34956 Tuzla, Istanbul, Turkey

[2]Sabanci University Nanotechnology Research and Application Center, 34956 Tuzla, Istanbul, Turkey

[3]School of Engineering, Computing and Mathematics, Oxford Brookes University, College Cl, Wheatley, Oxford, OX33 1HX, UK

[4]Advanced NEMS Laboratory, École Polytechnique Fédérale de Lausanne (EPFL), CH-1015 Lausanne, Switzerland

[5]Department of Biomedical Engineering and Health Systems, KTH Royal Institute of Technology, SE-141 57 Stockholm, Sweden

[6]Department of Materials, University of Oxford, Parks Road, Oxford OX1 3PH, UK

[7]Center of Excellence for Functional Surfaces and Interfaces for Nano-Diagnostics (EFSUN), Sabanci University, Orhanli, 34956, Tuzla, Istanbul, Turkey

*E-mail of corresponding authors: mghorbani@sabanciuniv.edu, itzanakis@brookes.ac.uk and ali.kosar@sabanciuniv.edu

1   **Abstract:**

2   This study introduces the first experimental analysis of shear cavitation in a microscale Backward-

3   Facing Step (BFS) configuration. It explores shear layer cavitation under various flow conditions

4   in a microfluidic device with a depth of 60 μm and a step height of 400 μm. The BFS configuration,

5   with its unique characteristics of upstream turbulence and post-reattachment pressure recovery,

6   provides a controlled environment for studying shear-induced cavitation without the complexities

7   of other microfluidic geometries. Experiments were conducted across four flow patterns:

8   inception, developing, shedding, and intense shedding, by varying upstream pressure and Reynolds

9   number. The study highlights key differences between microscale and macroscale shear cavitation,

10   such as the dominant role of surface forces on nuclei distribution, vapor formation, and distinct

11   timescales for phenomena like shedding and shockwave propagation. It is hypothesized that vortex

12   strength in the shear layer plays a significant role in cavity shedding during upstream shockwave

13   propagation. Results indicate that increased pressure notably elevates the mean thickness, length,

14   and intensity within the shear layer. Instantaneous data analysis identified two vortex modes

15   (shedding and wake modes) at the reattachment zone, which significantly affect cavitation

16   shedding frequency and downstream penetration. The wake mode, characterized by stronger and

17   lower-frequency vortices, transports cavities deeper into the channel compared to the shedding

18   mode. Additionally, vortex strength, proportional to the Reynolds number, affects condensation

19   caused by shockwaves. The study confirms that nuclei concentration peaks in the latter half of the

20   shear layer during cavitation inception, aligning with the peak void fraction region.

21   **Keywords**: Hydrodynamic cavitation; Microfluidic device; Backward-Facing Step (BFS);

22   Shedding mode; Wake mode

23

I. Introduction

Cavitation is a phenomenon triggered by a localized reduction in the liquid pressure below its saturation level, which results in an abrupt phase transition from liquid to vapor. This transition is often accompanied by a bubble collapse event and generation of shock waves and liquid jets. Among the various types of cavitation, Hydrodynamic Cavitation (HC) emerges as a significant area of interest attracting attention from both industry and academia due to its diverse applications and wide applicability in various engineering fields. In HC, cavitation arises from a localized increase in the flow velocity, resulting in static pressure drops below the vapor pressure (Venturi effect). This leads to the formation, growth, and subsequent violent collapse of vapor-filled cavities as the fluid pressure is recovered[1].

To gain a deeper understanding of the underlying mechanisms and to harness the potential of HC for practical applications, the investigation of this phenomenon at the microscale level is crucial. By controlling experimental conditions at this level, it is possible to change variables and observe cavitation behavior in detail[2–4]. The localized and intense nature of microscale cavitation also offers unique opportunities for developing innovative technologies in energy[5], biomedical treatments[6], and materials processing[7]. Recent studies have provided profound insights into this concept, and contributed to fundamental knowledge about scale effects, cavitation dynamics, operational conditions[2], and device configurations[8] essential for effective HC control in microscale. These achievements were made mostly by extensive experimental studies that covered major parameters such as device dimensions and geometries[2], fluid properties, surface engineering[9], and operation conditions[4]. Except for the case of bluff bodies[10], HC investigations in these studies were mostly limited to the use of restrictive flow elements, such as micro-orifices[11], microchannels[2,3], and venturis[12], where a sharp local drop in the flow pressure caused cavitation

1   inception. The unique characteristics of the BFS configuration, including the influence of the

2   upstream turbulent boundary layer and the pressure recovery after reattachment, distinguish its

3   cavitation mechanism from those observed in other microfluidic geometries. In particular, the

4   microscale BFS configuration provides a controlled environment for studying the effects of shear-

5   induced cavitation without the complexities of multiple interacting separation bubbles or the

6   formation of sheet cavities.

7   A critical yet underexplored aspect in microscale HC studies is the role of shear layer cavitation.

8   Shear flow refers to a type of fluid flow where layers of fluid move past one another with different

9   velocities, which generates a gradient in the velocity across the flow direction. In shear flows, the

10   velocity gradient between adjacent fluid layers is a key factor that can lead to instability and the

11   formation of coherent structures. One prominent example is the Kelvin-Helmholtz (KH)

12   instability, which occurs when there exists a relative velocity between two parallel fluid layers.

13   This instability results in the growth of vortices, which can merge to form larger coherent

14   structures, which plays a crucial role in the development of turbulence. Streamwise structures

15   aligned with the flow direction are also influenced by the mean flow profile and can contribute to

16   the overall dynamics of the shear flow, thereby affecting mixing and transport processes[13].

17   Cavitation in shear layers is closely related to the low-pressure core of vortices present in turbulent

18   shear layers[14,15]. The streamwise and spanwise vortices in the shear layer are key factors in

19   cavitation inception. The presence of spanwise vortices was found to be important in explaining

20   the Reynolds number dependence of the cavitation inception index[16] . Previous studies extensively

21   covered the onset of cavitation within the vortical regions of turbulent shear layers in Backward-

22   Facing Step (BFS) configurations[14,17–19]. A recurring theme across these studies is the strong link

23   between cavitation inception and pressure fluctuation peaks within the Quasi-Streamwise Vortices

4

Physics of Fluids

1   (QSVs). For example, Allan et al.[17] conducted experiments in a water tunnel to examine how

2   nucleation affects cavitation inception within a high Reynolds number shear layer formed behind

3   a BFS. Their findings revealed that following cavity collapse microbubbles dispersed throughout

4   the shear layer. Additionally, incipient bubbles became trapped within the recirculation zone,

5   which created favorable locations for renewed nucleation, ultimately leading to the development

6   of sustained cavitation. In another study, Agarwal et al.[15] examined the dynamic pressure field and

7   distribution of nuclei within and around QSVs to understand cavitation inception and the statistical

8   variations in pressure fluctuations near a shear layer behind a BFS. Their findings consistently

9   linked void fraction size and shape with intermittent low-pressure zones, which were preceded by

10   axial stretching of vortices and followed by contraction. They observed that an increase in

11   Reynolds number (Re) resulted in reduced viscous diffusion of the vortex core, causing a decrease

12   in the QSV diameter and pressure minima under the same straining rate.

13   The vorticity structures within the shear layer potentially led to vapor development and escalation

14   in vapor production within the separated region of the flow which occurs due to an adverse pressure

15   gradient encountered downstream of the step. In a recent investigation by Bhatt et al.[20], the

16   dynamics of cavitation within the BFS configuration was scrutinized employing X-ray

17   densitometry and high-speed imaging. They explored how the Reynolds (Re) number influenced

18   various cavity characteristics and behavior of the shear layer in the presence of a substantial vapor

19   void fraction. Their findings revealed a mild effect of Re number on mean cavity lengths.

20   Additionally, they observed an adverse flow front resembling a shockwave, which advanced

21   towards the step and ultimately dissipated the cavity. In another study, Maurice et al.[21] investigated

22   the dynamics of cavitation in a test section incorporating a BFS. They utilized the high-speed x-

23   ray attenuation technique synchronized with pressure fluctuation measurements to examine how

1 changes in void fraction dynamics affected wall pressure fluctuations and vortex behavior at

2 different levels of cavitation. Their findings revealed that pressure waves generated during extreme

3 events significantly modified the flow pattern and structure upon impact with the step wall. In a

4 study by Lv et al. [22] the influence of hydrophobic surfaces on pseudo-cavitation within a backward

5 step configuration was investigated for different Reynolds numbers, where the bottom surface was

6 designed to have a hydrophobic nature. In contrast to the typical cavitation phenomenon in

7 backstep devices where the inception occurs within the shear layer due to the free gas nuclei

8 coming with the upstream flow, the Lv's study used gas nuclei trapped on the hydrophobic surface

9 to incept cavitation. According to their results, inception occurred in the minimum pressure region

10 of the hydrophobic surface, and a peak bubble size occurred for a specific Re number, while bubble

11 oscillation continuously increased with Re number. Recently, Maleki et al.[23] numerically

12 investigated shear cavitating flow and its interaction with a turbulent separation bubble (TSB) in

13 a microscale BFS domain, employing compressibility effects and finite mass transfer for a more

14 comprehensive analysis. Their work shed light on the influence of cavitation on the mean flow

15 characteristics and dynamics of the coherent structures. They observed that vapor development

16 within the shear layer and its collapse close to the reattachment can have notable consequences on

17 the shape and dynamics of vortices within the shear layer and pressure spectral content within the

18 reattachment. While numerical simulations offer valuable insights, experimental validation under

19 various conditions and scales is crucial for a deeper understanding of the complex physics

20 governing shear cavitating flows in BFS configurations.

21 Understanding the mechanisms behind the generation of cavitation in shear layers is crucial for

22 the design and optimization of fluidic systems and flow control. The present study investigates

23 cavitation inception mechanisms and development of cavitating flow patterns using new

1   generation HC-on-a-chip microfluidic devices with a BFS. This study aims to elucidate the distinct

2   behavior of microscale shear cavitation compared to its macroscale counterpart. Key areas of focus

3   include the dominance of surface forces and their impact on nuclei distribution and vapor

4   development, as well as the significantly different timescales for phenomena such as shedding and

5   shockwave propagation. Furthermore, we hypothesize that the strength of vortices within the shear

6   layer plays a crucial role in cavity shedding during upstream shockwave propagation from the

7   reattachment region. It is expected that this study will open new research directions for

8   investigating the role of HC generation on the possible effects of cavitation bubble collapses in

9   chemical and mechanical engineering applications.

10

11   **II.   Experimental Overview**

12   *A. Device Fabrication and Configuration*

13   Experiments were conducted on a microfluidic HC-on-a-chip device (reactor) with a BFS

14   configuration, whose dimensions and geometry are shown in Figure 1. The reactor consisted of

15   two primary sections which were the microchannel and the extension channel. The inlet port, with

16   a diameter of 1000 μm, was connected to the microchannel, which had dimensions of 400 μm in

17   height, 4000 μm in length, and 60 μm in depth. Following the microchannel, there was an extension

18   channel where cavitating flow patterns were observed. The dimensions of the extension channel

19   were 800 μm in height, 4000 μm in length, and 60 μm in depth. The outlet port, with a diameter

20   of 1000 μm, was located at the end of the extension channel. The reactor was fabricated using a

21   process flow derived from semiconductor microfabrication techniques. The major fabrication steps

22   included a silicon (Si) wafer grinding, silicon dioxide (SiO_2) coating, photolithography, SiO_2 and

23   Si etching, protective layer deposition, wet etching, and piranha cleaning as illustrated in Figure

1   2. In the final step, the Si-based substrate was cleaned and anodically bonded to a Borofloat 33

2   glass to form a high-pressure-resistant semi-transparent closed channel structure for visualization.

3   The detailed fabrication process flow can be found in the previous study[8].
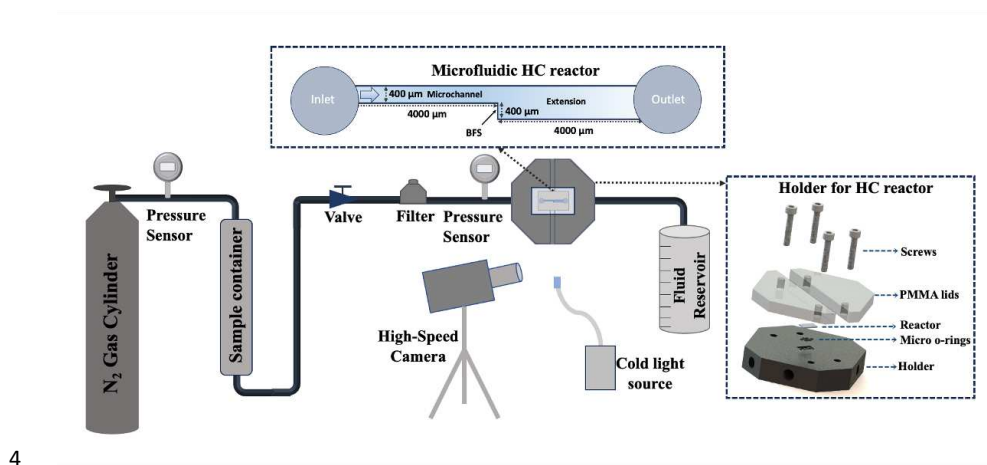
4

5   *Figure 1 Schematic of the experimental setup, microfluidic HC reactor, and holder for HC reactor.*
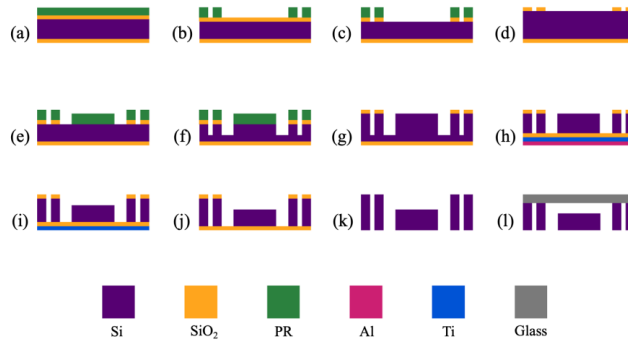
6

7   *Figure 1 Fabrication process flow for the microfluidic HC reactor. a) Four-micrometer photoresist casting on a 500nm silicon*

8   *dioxide (SiO$_2$)-coated Silicon (Si) wafer. b) Maskless lithography process of the features drawn by Layout Editor Software. c)*

9   *Etching of SiO$_2$ layer with an ICP-based high-density plasma source (SPTS APS). d) Stripping of the photoresist. e) Lithography for*

1 *the fabrication of the ports. f) Deep Reactive Ion Etching (DRIE) for the etching of Si. g) Photoresist stripping. h) 10 nm of*

2 *Titanium (Ti) and 2 μm of Aluminum (Al) sputtering on the backside of the Si wafer to increase its durability. Wet etching and*

3 *second DRIE to form the inlet and outlet. i) Wet etching for the removal of Al. j) Wet etching of Ti. k) Wet etching of SiO₂ layer. l)*

4 *Anodic bonding of the glass following etching of SiO₂ layer.*

5   *B. Experimental Setup and Procedure*

6 The experimental setup, as depicted in Figure 1, comprised a pressurized pure N_2 gas cylinder

7 (BOC, UK), a sample container (Swagelok, Erbusco, Italy), pressure sensors (Omega, Manchester,

8 UK, with an accuracy value of $\pm 0.25\%$ and a range of up to 3000 psi), stainless steel tubing

9 (Swagelok, Erbusco, Italy), and an aluminum holder. The aluminum holder featured a grove with

10 a depth similar to that of the reactor. The reactor was further equipped with convenient inlet/outlet

11 connections sealed via micro-O-rings. To ensure optimal sealing and safety, the reactor was then

12 tightly sandwiched with transparent Poly(methacrylic acid methyl ester) (PMMA) lids. The

13 experiments were initiated by feeding the sample container with the working fluid (in this study:

14 de-ionized water). Pressurized N_2 gas was then released in a controlled manner using a pressure

15 regulator to compress and convey the fluid into the system. The fluid was filtered by a 15 μm

16 nominal pore size micro-T-type filter (Swagelok) to remove undesirable particles before entering

17 the package. The upstream pressure was monitored by a pressure sensor located just before the

18 holder. Different flow patterns were generated by increasing the inlet pressure, while the outlet

19 pressure was kept constant as atmospheric pressure. The fluid was collected in a reservoir with 20

20 mL volume after passing through the reactor to calculate the volumetric flow rate. The experiments

21 were performed at four different inlet pressures corresponding to four different flow patterns which

22 were characterized by four cases in this study, namely Case I, Case II, Case III and Case IV. The

23 details of experimental parameters regarding flow condition, flow parameters, and nondimensional

24 numbers, including Re numbers ($Re_D = UD_h/\nu$), where Re_D is the Re number based on the

1   hydraulic diameter (D_h), U is the mean velocity within the microchannel calculated based on the

2   volumetric flow rate, and ν is kinematic viscosity) and cavitation numbers ($\sigma = (p_{in} -$

3     $p_{sat})/(\frac{1}{2}\rho_w U^2)$, where p_{in} is inlet pressure, p_{sat} is vapor saturation pressure of water and ρ_w

4   shows water density) are provided in Tables 1 and 2 (ρ_v and μ_v represent vapor density and

5   dynamic viscosity, respectively).

6   Multiple runs of the experiments were performed under strict control over experimental conditions

7   to evaluate the consistency of our results. Specifically, the experiments were performed at least

8   three times to ensure the consistency and reliability. The sensors used in this study were calibrated

9   regularly before the experiments to minimize any potential measurement deviations. A detailed

10   uncertainty analysis is also included in Table 3, which implies the potential errors arising from

11   microfabrication and measurements. The variability of the results was quantified by calculating

12   the percentage uncertainty. The uncertainty propagation method was used for this[24], and error

13   values of sensors are received from the manufacturer's datasheet.

14

Table 1 Fluid properties and flow conditions of the current study.

$\rho_w \left[\frac{kg}{m^3}\right]$	$\rho_v \left[\frac{kg}{m^3}\right]$	$p_{sat}[MPa]$	$\mu_w \left[\frac{Ns}{m^2}\right]$	$\mu_v \left[\frac{Ns}{m^2}\right]$	$\gamma \left[\frac{N}{m}\right]$	$T_{ambient}[K]$	$p_{outlet}[MPa]$
998.2	0.554	2.34×10^{-3}	0.9×10^{-3}	0.742×10^{-6}	0.072	293.16	0.1

15

16

Table 2 Inlet pressure and flow regimes in the current study.

	Case I	Case II	Case III	Case IV
$p_{in}[MPa]$	2.38	2.90	3.79	4.83

σ	3.183	3.074	2.896	2.155
Re_D	3,820.1	4,291	5,054	6,633

1

2

Table 3 Uncertainties in experimental parameters

Uncertainty	Error
Flow rate	±1.3%
Cavitation number	±6.5%
Reynolds number	±5.6%
Hydraulic diameter	±3.4%
Pressure drop	±0.3%

3

4   *C. Visualization and quantification of void fraction*

5   High-speed visualizations were performed in-situ using a high-speed camera (Fastcam SA-Z 2100

6   K (Photron, UK)) equipped with a Navitar 12 × zoom lens (0.5 × 0.009–0.051NA 1–50012) with

7   resolution as low as 6.66 μm and depth of field ranging from 0.19 – 6.17 mm. The cavitation zone

8   inside the reactor was illuminated by a high-power cold light source (Karl Storz Power LED 175,

9   Germany) from the front. The cavitation phenomena were recorded at a rate of up to 10^5 frame per

10   second (fps). In order to maintain desirable spatial resolutions, the images were acquired at a

11   frequency of 80000 Hz at 0.23 megapixels in this study. The image resolution was 752×312 with

12   an optical magnification of 0.27 mm px^{-1}, and the image depth was 8 bit. For all the series of

11

1   images obtained with the high-speed camera, camera settings for brightness and contrast were kept

2   constant and equal. The details regarding the data analysis are included in Appendix A.

3

4

5   **III.   Results and Discussion**

6   *A. Flow Regimes, Inception, and Nuclei Content*

7   In this study, four distinct flow regimes were identified by varying the inlet pressure and

8   maintaining atmospheric pressure at the outlet. These regimes are shown as instantaneous

9   snapshots in Figure 3 and are also summarized by casting their corresponding flow conditions.

10   Inlet pressures were systematically selected based on preliminary tests to encompass the full range

11   of cavitation regimes, from inception to intense shedding. This approach allowed for a

12   comprehensive analysis of shear cavitation dynamics within the microscale backward-facing step

13   geometry. In turbulent shear cavitation, cavitation inception (case I) is associated with the first

14   appearance of cavitation or the first occurrence within quasi-streamwise vortices (QSV) as they

15   are stretched between spanwise vortices of the shear layer[15]. As the inlet pressure increases, the

16   mean kinetic energy of the flow also rises, which leads to a decrease in the cavitation number.

17   Consequently, more intense cavitation becomes visible with increasing inlet pressure. The primary

18   factor contributing to this observation is the strengthening of vortices and associated increase in

19   the local velocity within the shear layer. These strengthened vortices induce a significant drop in

20   local static pressure, creating conditions favorable for cavitation inception. In Case II, cavitation

21   preferentially develops near the middle of the shear layer and around the reattachment point,

22   aligning with the location of spanwise vortices (the vortices developed due to the Kelvin-

1   Helmholtz instability and velocity gradient within the shear layer). In Case III, a thicker and more

2   intense cavitation region forms closer to the step. Finally, Case IV exhibits intense shedding

3   cavitation encompassing the entire shear layer, with numerous bubbles present within the

4   separation bubble (the volume enclosed by the region of the separated flow) that are shed from the

5   main cavitation region.

6
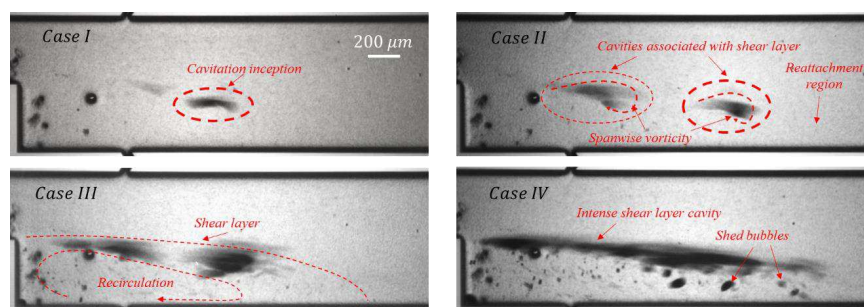
8   *Figure 3 High speed camera snapshots of different cavitating flow regimes in BFS configuration. Case I: inception, Case II:*

9   *developing, Case III: shedding, Case IV: intense shedding.*

10

11   Figure 4 depicts the development of vapor packets (cavitation) behind the BFS at various time

12   intervals and positions. These observations were made at the upstream pressure of 2.38 MPa,

13   which corresponds to the critical pressure for the first observation of cavitation on the reactor. The

14   complex flow patterns within the reactor, featuring different types of vortices and high shear stress

15   zones within the shear layer, act as nucleation sites for cavitation bubbles. These vortices and high

16   shear stress regions accelerate the rapid growth and collapse of cavitation nuclei, triggering

17   cavitation events. Several studies [14,15,20,21,25] reported cavitation inception within QSV structures.

1   The high-speed camera visualization shows that cavitation inception occurs after nuclei become

2   trapped within the shear layer. These bubbles likely originate from the upstream location of the

3   step or are remnants of previous cavitation collapses near the reattachment zone. As can be seen

4   in Figure 4, cavitation incepts within the shear layer formed behind the BFS. The inception process

5   involves the repeated formation and collapse of vapor bubbles, likely due to nuclei trapped in the

6   shear layer or fluctuating local pressure. [11,12,20–22] In some cases, these bubbles progress to larger

7   spanwise vortices within the shear layer. These bubbles have significant shape and size changes

8   before collapsing in high-pressure regions. Trapped nuclei first expand in low-pressure areas

9   within the shear layer, then rapidly contract and collapse upon entering high-pressure zones.

10 Furthermore, local variations in the shear layer, such as changes in the velocity gradients and

11 pressure fluctuations, influence the formation and collapse of these bubbles (Iyer and Ceccio,

12 2002).

13
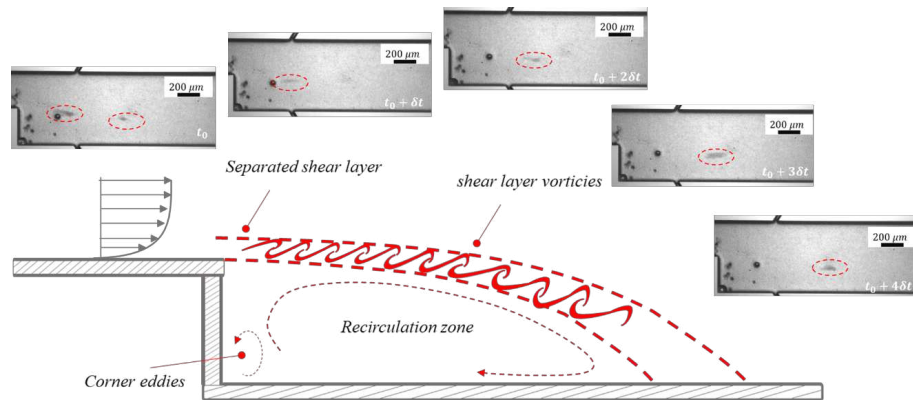
14

15   *Figure 4 Sequence of images extracted from high-speed videos showing the evolution of a discrete incipient cavity.*

16

14

1 The number and distribution of nuclei in the wake of the BFS significantly affects cavitation. When

2 these nuclei coincide with local low-pressure zones, cavitation intensifies in susceptible regions.

3 As shown in previous studies[17], a higher concentration of nuclei leads to more intense cavitation

4 within the shear layer. Based on the observations, it can be deduced that bubble collapses near the

5 reattachment zone significantly contribute to the nuclei population within the separation bubble.

6 These shed bubbles are primarily trapped within the separation bubble before re-entering the shear

7 layer and intensifying cavitation. Therefore, the focus is on quantifying the spatial distribution of

8 these bubbles within the separation zone to identify areas with the highest nuclei concentration.

9 Additionally, it is aimed to investigate the impact of the cavitation regime on the distribution and

10 fluctuations of these nuclei.

11 Figure 5 presents the time-averaged distribution of normalized nuclei concentration within the

12 separation bubble for various cavitation regimes. Nondimensional coordinates normalized by step

13 height are shown by $\tilde{x}$ and $\tilde{y}$. In the inception regime, most nuclei are concentrated in the region

14 defined by $\tilde{x} \sim 2 - 4$ and $\tilde{y} \sim 0.5$. As the pressure increases downstream of this region, vapor

15 bubbles primarily collapse here, generating new nuclei. These nuclei become trapped within the

16 recirculation zone and are then transported back to the center of the shear layer, triggering new

17 cavitation events. At a higher pressure of 2.9 MPa, the nuclei level within the separation bubble

18 increases. Additionally, a high concentration of bubbles is observed not only in the second half of

19 the shear layer but also in the corner vortex and first half of the shear layer, which contributes to

20 cavitation within the first half of the layer at this pressure. At even higher upstream pressures, the

21 nuclei concentration further increases, particularly within the first half of the separation bubble.

22 Figure 6 depicts the root mean square (RMS) bubble concentration, which reflects the temporal

23 variations of bubble nuclei across the spatial domain. High RMS values correspond to regions with

1 a high average bubble concentration (as shown in Figure 5), indicating significant fluctuations in

2 bubble presence within these areas. The RMS values are remarkable across a large portion of the

3 separation bubble and downstream of the reattachment zone, suggesting a scattered distribution of

4 bubbles throughout these regions.
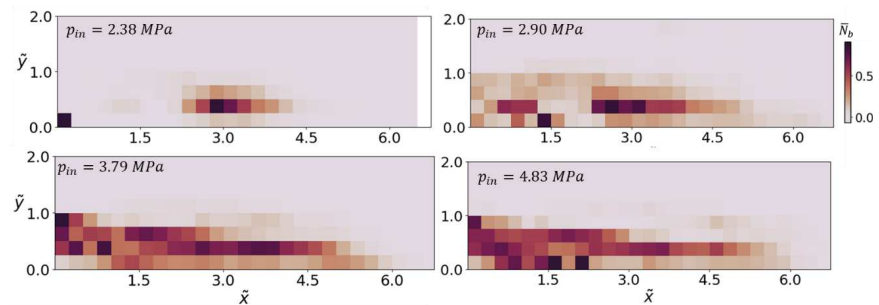
6 *Figure 5 Time averaged of spatial distribution of nuclei bubbles in the BFS separation bubble at four different upstream*

7 *pressures. The concentration in each discrete square region was obtained by summing the number of discrete bubbles in the*

8 *corresponding region over all time steps and dividing with the number of time steps.*

9
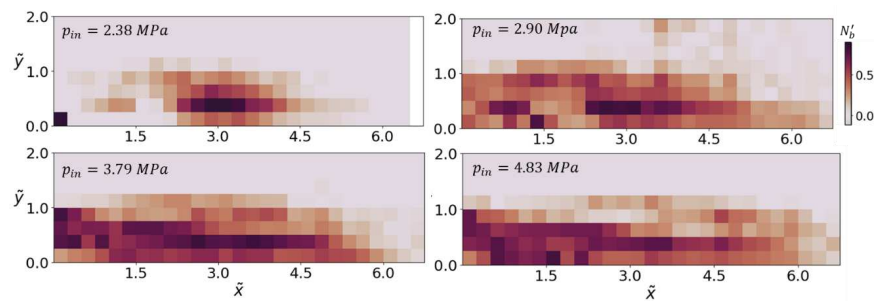
11 *Figure 6 Root mean square of spatial distribution of nuclei bubbles in the BFS separation bubble at four different upstream*

12 *pressures. The concentration in each discrete square region was obtained by summing the number of discrete bubbles in the*

13 *corresponding region over all time steps and dividing with the number of time steps.*

16

1

2

3   *B. Mean Characteristics of Void Fraction*

4   The mean and standard deviation of void fractions are presented in Figure 7 for all cases. It can be

5   seen that for all cases the maximum mean void fraction lies within the shear layer, and its intensity

6   and length increase for smaller cavitation number.

7   The root mean square (RMS) values of void fraction fluctuations generally exhibit a similar pattern

8   to the mean void fractions, with one notable exception observed for Case III. Here, the peak in the

9   mean void fraction (occurring near the step) does not coincide with the peak in void fraction

10   fluctuations, which is located within the middle region of the shear layer. This discrepancy suggests

11   that for Case III, while the average vapor content is highest near the step, the most significant

12   fluctuations (rapid changes in vapor content) occur within the shear layer. Furthermore, Cases III

13   and IV have noticeably higher void fraction fluctuations within the recirculation zone. This

14   observation aligns with the expectation that the number of shed bubbles from cavitation packets

15   increases as the cavitation number decreases (indicating more intense cavitation). These bubbles

16   likely contribute to the increased fluctuations observed within the recirculation zone.
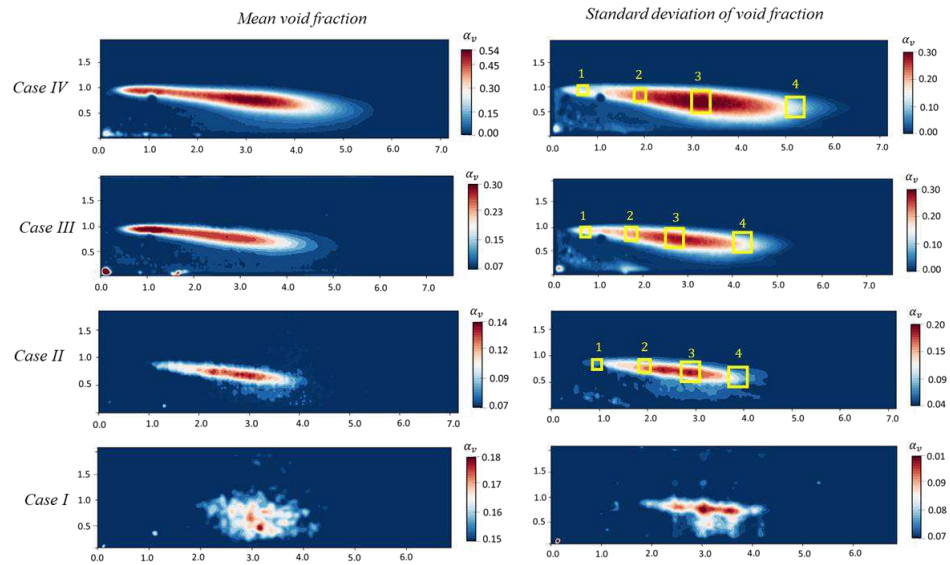
Figure 7 Contours of mean (left column) and standard deviation (right column) of void fractions for Cases I to IV. Red squares indicate the probes used for spectral analysis, numbered for easy reference. To enhance clarity, separate color bars with distinct value ranges are employed for void fraction data.

Figure 8(a) presents the maximum values of the mean void fraction ($\bar{\alpha}_{max}$) along the streamwise direction. These values offer valuable insights into the evolution of vapor content within the shear layer. As they are independent of transverse coordinate (y), they can be used to evaluate mean global behavior in each flow regime. As demonstrated by Maurice et al. [21], the cavitation region can be segmented into three distinct zones: cavitation generation which is characterized by the increase in void fraction, eddy transport region where the void fraction is almost constant and cavities are transported with shear layer vortices, and condensation associated with decrease in void fraction. Four cases of cavitation regimes are evaluated based on these cavitation zones.

1   The region of cavitation generation is typically associated with a rise in the maximum mean void

2   fraction along the streamwise direction (indicated by $\bar{\alpha}_{max}$ in Figure 8a). The observations for

3   Case IV reveal that this peak corresponds to the cavitation generation zone which lies in $(0 < \tilde{x} <$

4    $0.8)$. Interestingly, the width of this generation region expands with increasing cavitation number,

5   which implies that as the cavitation number increases (indicating less intense cavitation

6   conditions), cavitation occurs further downstream from the step. In Cases I and II, it is observed

7   that the area of peak void fraction aligns with the peak nuclei concentration observed in Figure 7,

8   indicating that the second half of the shear layer is the most susceptible one to cavitation and also

9   the location with the highest nuclei concentration during inception.

10   The region with relatively flat variations in the maximum mean void fraction $(\bar{\alpha}_{max})$ corresponds

11   to the zone with eddy transport for the cavitation bubbles. For Case IV, the plateau region $(0.8 <$

12    $\tilde{x} < 3.5)$ aligns with this transport zone. The width of this transport region exhibits a decrease with

13   increasing cavitation number (with moving of peak in generation downstream). This observation

14   can be explained by the fact that cavitation inception occurs further downstream within the shear

15   layer as the cavitation number increases. Moreover, it can be observed that the condensation starts

16   almost at the same location $(\tilde{x} = 3.5)$ for all cases, while the slope of $\bar{\alpha}_{max}$ in generation and

17   condensation significantly decrease with an increase in the cavitation number.

18   To further investigate differences in characteristics of shear cavitation for different regimes, the

19   mean shear cavitation thickness within the shear layer was used as the characteristic length scale

20   using the following equation [26]:

21    $L_{\bar{\alpha}}(\Delta x, \tau) = \int_{-h/2}^{h/2} R_{\alpha\alpha}(x, \Delta y) \, d\Delta y$ (1)

22   where the spatial correlation $(R_{\alpha\alpha}(x, \Delta y))$ is defined as:

1 $$R_{\alpha\alpha}(x, \Delta y) = \frac{\langle \bar{\alpha}(x_{ref}, y_{ref}) \bar{\alpha}(x_{ref}, y_{ref} + \Delta y) \rangle}{\alpha'_{rms}(x_{ref}, y_{ref}) \alpha'_{rms}(x_{ref}, y_{ref})}$$ (2)

2 In this equation, $\langle \rangle$ represents the ensemble average, $\bar{\alpha}$ is the temporal mean of the void fraction,

3 and α'_{rms} is the root mean square (RMS) of the void fraction fluctuations. Figure 8(b) depicts the

4 evolution of the estimated characteristic length scale, which is directly proportional to the

5 thickness of the vapor phase within the shear layer. For all cases, it is evident that the maximum

6 thickness occurs approximately at the midpoint of the shear layer ($\tilde{x} \approx 3.3$), which indicates that

7 the maximum cavitation thickness is attained before reaching the condensation region, where

8 subsequent condensation leads to a reduction in this thickness. Moreover, the thickness decreases

9 notably with an increase in the cavitation number (and simultaneously decreasing the Re number),

10 indicating a decrease in both the size and strength of spanwise vortices within the shear layer.

11
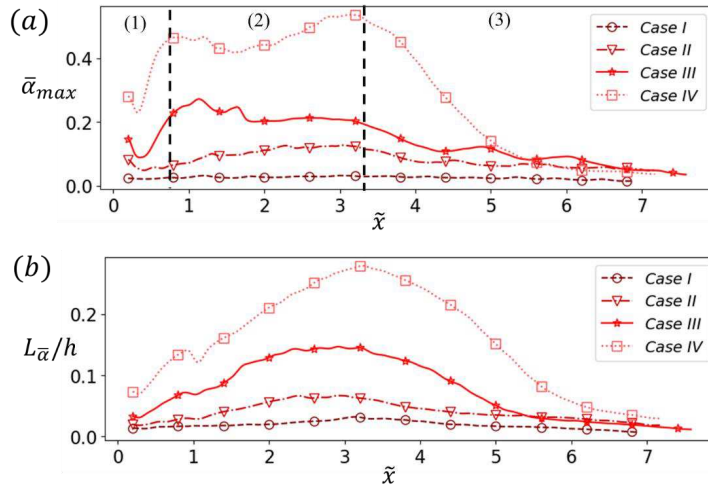
Figure 8 (a) Evolution of the maximum of the mean void fraction field (1, 2, and 3 show regions of the vapor generation, transport and condensation, respectively), and (b) Characteristic void fraction length-scale evolution along the longitudinal direction

Spatio-temporal correlation for the fluctuating void fraction field was calculated as (Weiss et al., 2015):

$$R_{\alpha\alpha}(\Delta x, \tau) = \frac{\langle \alpha'(x_{ref}, t_{ref}) \alpha'(x_{ref} + \Delta x, t_{ref} + \tau)\rangle}{\alpha'_{rms}(x_{ref}) \alpha'_{rms}(x_{ref} + \Delta x)} \tag{3}$$
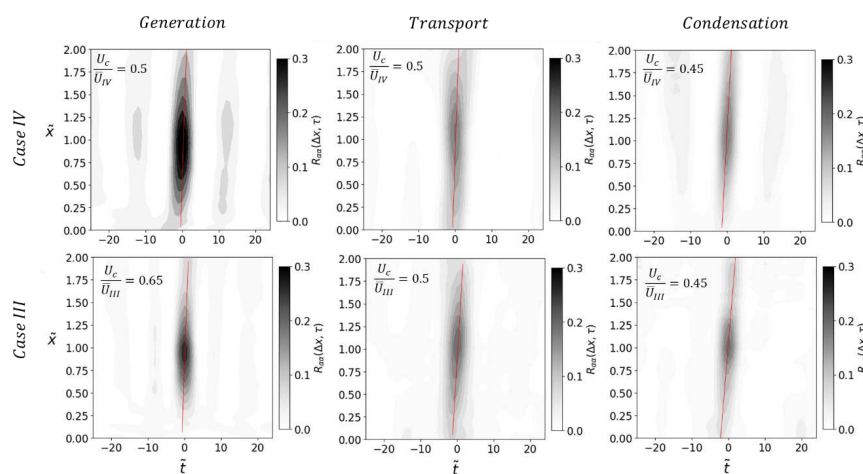
Figure 9 presents the spatio-temporal correlations for Cases III and IV. Spatio-temporal correlations are not considered for Cases I and II due to limitations in the data. Case II has a limited number of snapshots, hindering accurate estimation of these correlations. Additionally, the sparse and transient presence of void fractions, especially in Case I, makes tracking void movement impractical, further complicating the reliable estimation of spatio-temporal correlations. Spatio-temporal correlation quantifies the statistical relationship between fluctuations in void fraction at

21

1 different spatial locations and across time within the cavitating shear layer, which helps to

2 understand how variations in the vapor content are interconnected. The normalized convective

3 velocities were approximated by fitting a linear function to the local maxima observed in the

4 correlation functions. The results reveal that the mean convective velocities in both cases are

5 approximately half of the mean bulk velocity of the flow (particularly in transport zone). This

6 aligns with previous observations of convective velocities for coherent structures within free shear

7 layers [27], which decreases along the shear layer. This result confirms that the vapor is mainly

8 transported within these spanwise vortical structures.

9

10

11 *Figure 9 Spatio-temporal correlation of void fraction for Cases IV and III in three different regions which were obtained based on*

12 *Figure 8 (Generation: $0.0 < \tilde{x} < 2$, Transport: $2 < \tilde{x} < 4$, Condenstaion: $4 < \tilde{x} < 6$). The red line was obtained using linear*

13 *fitting of the correlation maxima. The slope of the line represents the mean convective velocity (U_c) of the void fraction in each*

14 *region. The normalized value of convective velocity (normalized by reference velocity in the corresponding case) is provided in*

15 *each plot.*

1   *C. Spatio-temporal Dynamics of void fraction*

2   The images from the high-speed camera are presented in Figure 10 for the upstream pressure of

3   4.83 MPa (Case IV) along with the spatio-temporal map of void fraction in this regime. Only time

4   series of Cases IV and III are studied here because the sparse and short-lived presence of void

5   fractions, especially in Case I, makes it difficult to follow their movement in the given temporal

6   resolution. The time interval between sequential images is 12.5 μs. As already discussed in the

7   previous section, pressure drops within spanwise vortices of the shear layer provide suitable

8   conditions for cavitation development. In the snapshot related to the time instance of t_0, separate

9   vapor packets along the shear layer are visible (indicated by 1, 2, 3 markers). In this case, the vapor

10   phase fills the spanwise vortical structures, which are connected to each other through QSVs.

11   Furthermore, many small bubbles (with sizes between $5\mu m$ to $20\ \mu m$) which are shed from the

12   large vapor packets within the shear layer are observed within the recirculation zone. These small

13   bubbles help in visualization of vorticity distributions and their variations within the recirculation

14   region. They also feed and reinforce cavitation at different locations within the shear layer. As

15   indicated in time instance $t_0 + \delta t$, recirculation region encompasses multiple clockwise and anti-

16   clockwise vortices, which have shape variation, merge and split as the reattachment is displaced

17   along the wall. In this time instance, vapor packet 1 develops which corresponds to the

18   development and growth of spanwise vortices associated with the packet. Meanwhile, a link of

19   vapor forms between the 1st and 2nd packets, demonstrating development of vapor towards

20   streamwise structures which connect two sequential spanwise structures. Once the separation

21   bubble reaches its maximum size, a vortex associated with vapor packet 3 detaches from the

22   downstream end of the separation bubble. Prior studies[28–30] demonstrated that the length of the

23   separation bubble, particularly in turbulent flows, is primarily controlled via the balance between

1   forces exerted by the pressure field and Reynolds normal and shear stresses along the recirculation

2   zone or bubble boundary. The high Reynolds shear stress near the reattachment point promotes a

3   longer reattachment length. In contrast, both of the forces due to Reynolds normal stress and

4   pressure field act along the upstream direction. At lower Re numbers, viscous shear and normal

5   stresses dominate, while Reynolds stresses become negligible. Furthermore, Nadge and

6   Govardhan [30] reported that both Reynolds shear and normal stresses depend on the geometry and

7   Re number, while the pressure force component remains independent of step size. Any imbalance

8   in these forces, such as differences in the entrainment to the shear layer from the recirculation zone

9   and re-entrainment [28], can trigger a shedding mechanism at the reattachment point. This event is

10   coupled with the displacement of the reattachment, change in the size and shape of the vortices

11   within the recirculation and merging of spanwise vortices within the shear layer which corresponds

12   to the 1st and 2nd vapor packets within the shear layer. In the light of the image sequence, the

13   velocity of the shed vapor at the reattachment (packet 3) can be approximated as $\approx 32.6\ m/s$.

14   After reestablishment of the reattachment in the time instance of $t_0 + 3\delta t$, cavitation is developed

15   within the shear layer so that the shear layer is filled with vapor. Then, the reattachment gradually

16   moves downstream. At the same time, vapor packets move along the wall at the front of the

17   reattachment. The time slot between $t_0 + 4\delta t$ and $t_0 + 7\delta t$ demonstrates that vapors cannot pass

18   through the reattachment within the shed vortices, which suggests that the shed vortices are not

19   strong enough to sustain the required low pressure in their cores for carrying vapor packets deep

20   into the channel. Consequently, the vapor condenses immediately in front of the reattachment

21   zone, forming small bubbles that are dispersed and carried to the upstream location by the reentrant

22   jet. To elucidate the mechanism by which vapor collapse at the end of the shear layer leads to

23   bubble shedding and their subsequent transport and distribution within the separation bubble,

Physics of Fluids

AIP Publishing

1   movies visualizing the bubble tracking process are provided. Movie 1 (Multimedia view) tracks

2   the generated bubbles within the separation bubble. Most of these bubbles rejoin the shear layer at

3   various locations, primarily in the middle region (interface between the clockwise and

4   counterclockwise vortices within the recirculation zone). Furthermore, the images reveal minimal

5   displacement of the reattachment point and variation in the size and shape of the separation bubble

6   during this time period (compared t_0 to $t_0 + 3\delta t$). This suggests the presence of smaller shed

7   vortices during this time, which is further displayed in the spatio-temporal map of void fraction in

8   Figure 10(a).

9   As the time progresses to $t_0 + 8\delta t$, the vortices within the recirculation zone and spanwise

10   vortices within the shear layer continue to develop and convect. Consequently, a relatively large

11   vapor packet located within a shear layer vortex begins to break apart and detach from the

12   separation bubble. The collapse of the large vapor packet and resulting pressure wave significantly

13   reduce the vapor intensity and shear layer thickness between time slot $t_0 + 9\delta t$ and $t_0 + 11\delta t$. In

14   the instance of $t_0 + 12\delta t$, the recirculation zone undergoes a dramatic change. A large

15   recirculation vortex, along with vapor trapped within the shear layer, begins to detach from the

16   separation bubble (TSB). This detachment carries a significant portion of vapor with the vortex,

17   initiating a new cycle.

1   *Figure 10 Time sequence of cavitation development and dynamics for the upstream pressure of 4.83MPa ($\delta t = 1.25\mu s$). The*

2   *initial stages (frames 1-4) utilize markers (1, 2, and 3) to track the movement of distinct vapor packets, each associated with a*

3   *separate shear layer spanwise vorticity. For better clarity, some vorticities within the shear layer, recirculation zone, and region*

4   *after reattachment (shed vorticity) are highlighted with dashed red lines. The corresponding time interval within the spatio-*

5   *temporal map is highlighted by a red overlay.*

6

7   Figure 11 demonstrates that the shedding mechanisms during the time slot between (t_0 to $t_0 +$

8    $3\delta t$) and ($t_0 + 12\delta t$ to $t_0 + 15\delta t$) differ significantly from the mechanism observed during the

9   time slot between $t_0 + 4\delta t$ and $t_0 + 11\delta t$. These two distinct shedding behaviors closely resemble

10   the two modes of wake and shear shedding identified by Hudy et al. [31] and observed by Maurice

11   et al. [21]. Hudy et al. [31] identified two distinct shedding modes in the flow behind a step. In the wake

12   mode, large, and strong vortical structures detach and convect downstream, accompanied by more

13   energetic pressure fluctuations along the wall (characterized by large peaks and valleys).

14   Conversely, the shear mode is characterized by the continuous growth and merging of spanwise

15   vortices within the shear layer. Here, vortices shed from the shear layer once their size reaches a

16   size comparable to the step size. As shown by Hudy et al. [31], this mode is associated with less

17   dramatic pressure fluctuations, characterized by smaller peaks and valleys which suggests weaker

18   vortex shedding. The vapor distribution observed in Figure 11 aligns perfectly with these distinct

19   shedding modes. Figure 11 provides two specific time instances, each relevant to a particular mode.

20   In the wake mode (Figure 11, left), separate packets of vapor reside within the large vortical

21   structures. This coincides with the high-pressure peaks observed between the vapor packets and

22   low-pressure valleys within them. In contrast, in the shear mode (Figure 11, right), less intense

23   vapor fills the entire shear layer (including the vortices). Additionally, the recirculation region in

24   this mode consists of small and randomly oriented vortices. Comparable shedding mechanisms

27

1   were identified in our recent numerical investigation[23] of cavitating flow within a BFS

2   microchannel. Two shedding modes (coexisting with slow breathing motions) were observed: a

3   high-frequency mode characterized by small vortex shedding at the end of the separation bubble,

4   and a low-frequency mode associated with larger reattachment region excursions.

5   Our findings suggest that the wake mode is most likely initiated by the pressure wave generated

6   during the collapse of the large vapor packet at the downstream end of the shear layer ($t_0 + 8\delta t$).

7   This observation agrees with the results of a previous study by Maurice et al. [21]. They reported a

8   similar wake mode triggered by vapor collapse downstream of the reattachment point, followed

9   by pressure wave generation and propagation upstream towards the step. As previously discussed,

10   the pressure wave generated by the collapse at $t_0 + 8\delta t$ is insufficient to fully condense the vapor

11   within the strong spanwise vortices of the shear layer. It can, however, cause a marginal

12   condensation effect. Despite this limitation, the pressure wave possesses enough strength to disturb

13   the shear layer and recirculation zone, triggering a breakdown of the recirculation from its

14   midsection ($t_0 + 12\delta t$). This stands in contrast to the shear mode, where the shed vortices at the

15   reattachment point are the same vortices that develop within the shear layer. Consequently, they

16   show the frequency of the same order as the spanwise vortices of the shear layer. The spatio-

17   temporal map in Figure 10(a) further illustrates the distinct vortex shedding behavior observed in

18   the wake and shear modes. In the shear mode, vortex shedding at the reattachment point has a

19   relatively high frequency with a smaller amount of vapor penetration into the channel. Conversely,

20   the wake mode is characterized by significantly lower shedding frequency and a more random

21   shedding pattern (frequency of around ~60 kHz versus ~300 kHz in the case shear mode). This

22   behavior, combined with the stronger shed vortices associated with the wake mode, leads to a

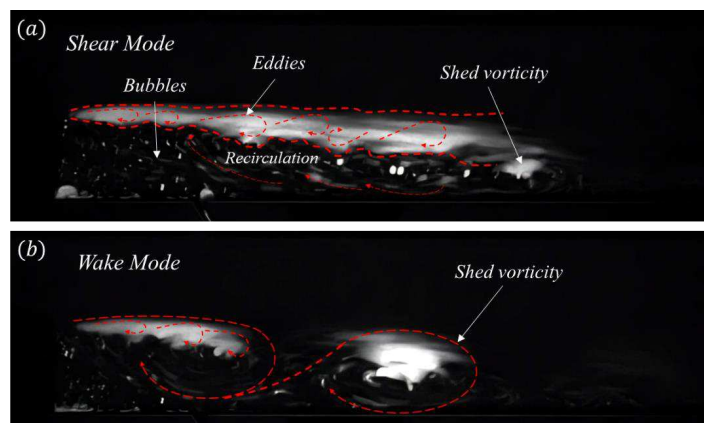23   larger penetration of vapor within the channel.

1

2   *Figure 11 Instantaneous results showing the (a) wake mode and (b) shear mode of vortex shedding in BFS cavitating flow.*

3

4   Figure 12(b) presents time instances of cavitation development for an upstream pressure of 3.79

5   MPa (corresponding cavitation and Re number given in Table. 2). Similar to the case of 4.83 MPa,

6   both wake and shear shedding modes are observed at this pressure. However, some notable

7   differences exist between the two upstream pressure conditions. As illustrated in previous studies

8   [32], a reduction in Re number generally leads to a decrease in the mean reattachment length

9   compared to the case with a higher Re number. This trend is also evident in the spatio-temporal

10   map provided in Figure 12(a). The vapor content within the channel and shear layer is significantly

11   lower at 3.79 MPa compared to the case with a higher Re number (Figure 12). This decrease is

12   primarily attributed to the weakened strength of the vortices within the shear layer at a lower Re

13   number. Consequently, even during the shear mode, the vapor is unable to fully occupy the shear

14   layer (t_0). The collapse of the vapor packet within the shear layer near the reattachment point ($t_0 +$

15   δt) is accompanied by a propagating condensation wave and a significant reduction in vapor

29

1   content within the shear layer ($t_0 + \delta t$ to $t_0 + 4\delta t$). Notably, condensation in this case appears to

2   be much more pronounced compared to the higher Re number case. This increased sensitivity to

3   pressure waves can be attributed to the weaker strength of the spanwise vortices within the shear

4   layer at lower Re number. This weakness is caused by a smaller velocity gradient across the width

5   of the shear layer. Consequently, the vortices are unable to generate strong local pressure drops

6   within the shear layer, making vapor more susceptible to condensation when a pressure wave

7   propagates through the medium. As discussed earlier, the presence of shed bubbles within the

8   recirculation zone plays a crucial role in facilitating the development of new cavities within

9   susceptible regions of the shear layer. Bubbles primarily originate from the shear mode regime,

10   where small vapor collapses occur near the reattachment point. In contrast, during the wake mode,

11   the vapor is transported further downstream and predominantly condenses far away from the

12   recirculation zone (see $t_0 + 11\delta t$). This large distance of condensation from the recirculation

13   prevents the generated bubbles from rejoining the shear layer via the reversed flow, thereby

14   effectively removing them from the region where they could contribute to the new cavity formation

15   (the velocity of the represented wake vorticity is approximately 17.3 m/s). Movie 2 (Multimedia

16   view) reveals that most of the shed bubbles successfully return to the shear layer, facilitating the

17   regeneration of cavitation within the layer after condensation ($t_0 + 5\delta t$). This observation aligns

18   with the behavior observed in the higher Re number case. Similar to the previous case, the shear

19   mode is followed by the wake mode. As discussed earlier, the pressure wave generated during the

20   final stage of the shear mode triggers the wake mode ($t_0 + 7\delta t$). However, in this case, the vapor

21   within the wake vortices condenses before reaching the end of the channel, which suggests that

22   the wake vortices in this case are weaker compared to those observed at higher Re number (first

23   case). This difference in the strength is linked to the lower mean pressure within the channel at

AIP
Publishing

1   3.79MPa compared to the first case. Furthermore, the spatio-temporal map of void fraction in

2   Figure 12(a) does not exhibit a clear distinction between the shear and wake modes at 3.79 MPa,

3   which is likely due to the weaker wake vortices and their limited impact on vapor transport
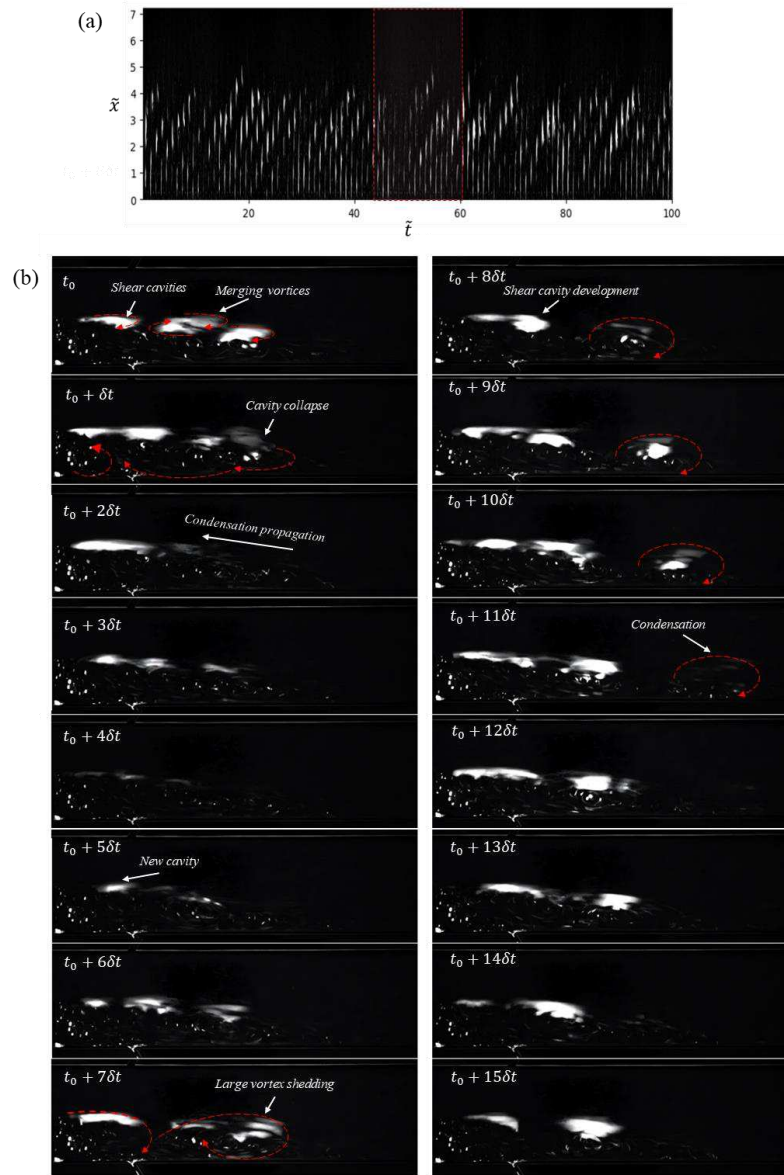
4   compared to the Case IV.

5

6

1

1   *Figure 12 Time sequence of cavitation development and dynamics for upstream pressure of 3.79 MPa ($\delta t = 1.25\mu s$). For better*

2   *clarity, some vorticities within the shear layer, recirculation zone, and region after reattachment (shed vorticity) are highlighted*

3   *with dashed red lines. The corresponding time interval within the spatio-temporal map is highlighted by a red overlay.*

4

5   The spatio-temporal map of the void fraction is provided in Figure 12(a). As can be seen, incidents

6   with deep penetration of vapor packets within the channel are apparent, while a long period of

7   almost uniform small penetrations can be observed. These results suggest that phase transition

8   within the shear layer changes the strength and dynamics of the shed vortices at the end of the

9   shear layer.

10   Figure 13 illustrates a schematic of shear and wake mode in shear cavitating flow, which includes

11   more details about cavitation dynamics in these modes. The shear mode (Figure 13(1)) includes a

12   developed separation bubble. As mentioned, this mode is associated with small vortex shedding

13   and small collapses which do not release enough energy to have a remarkable influence on the

14   vapor within the shear layer. This shedding continues for a while (depending to the flow condition)

15   until development and movements of eddies within the shear layer leads to a collapse of a large

16   amount of vapor at the end of the shear layer (Figure 13(2)). The speed of a shock wave is governed

17   by the pressure ratio across the wave and the thermophysical properties of the medium. While

18   analytical relations exist for ideal gases, predicting shock wave speed in complex two-phase media

19   becomes more challenging. For such cases, numerical simulations or experimental data are often

20   required to determine the shock wave speed. The Mach number (Ma), which represents the ratio

21   of the relative velocity of the shock wave to the local speed of sound in the undisturbed medium,

22   can be calculated using the relative shock wave speed and local speed of sound. In experimental

23   results the shock wave speed can be approximated as the speed of condensation front. The speed

33

1   of sound in two-phase mixture can be approximated using homogenous equilibrium model

2   (instantaneous heat transfer between phases) or homogeneous frozen model (no heat transfer

3   between phases). The general formulation that can be used by both model for estimation of local

4   speed of sound can be expressed as follows[1,20]:

5    $$\frac{1}{\rho_m c_i} = \frac{\alpha_i}{p_i}[(1-\epsilon_v)f_v + \epsilon_v g_v] + \frac{1-\alpha_i}{p_i^{1+\eta}}\epsilon_l g^* p_c^\eta \qquad (4)$$

6   where ρ_m shows the local mixture density, α_i and p_i are local void fraction and pressure, p_c is

7   critical pressure, $f_v, g_v, \eta,$ and g^* are material dependent parameters. $\epsilon_l = \epsilon_v = 0$ corresponds to

8   the homogeneous frozen model and $\epsilon_l = \epsilon_v = 1$ corresponds to the homogeneous equilibrium

9   model. From speed of condensation within the two-phase mixture in Figure 12 ($t_0 + \delta t$ to $t_0 +$

10   $5\delta t$) (Mach number, $Ma > 1$) it can be inferred that the collapse leads to a shockwave generation.

11   After the propagation of the shockwave through the shear layer condensation occurs. According

12   to our results, (Figures 13 and 12), the amount of condensation highly depends on the strength of

13   vortices within the shear layer, which is proportional to the velocity gradient across the shear layer

14   width and *Re* number. The condensation of the vapor within the shear layer triggers the wake mode

15   and breaking of the separation bubble (Figure 13(4)). Figures 13(5) and 13(6) show wake mode

16   shedding and subsequent development of the separation bubble, as was discussed earlier. Since

17   Cases III and IV exhibit comparable shedding mechanisms, a unified schematic will be presented

18   to illustrate the critical parameters governing this phenomenon in shear cavitating flow. The

19   upstream propagation of pressure waves triggered by the collapse of large vapor packets during

20   reattachment initiates the breakup of the separation bubble and transition to wake mode, which is

21   a notable finding, also supported by previous study of Maurice et al. [21]. This suggests that the

22   pressure wave propagation exacerbates the imbalance between effective forces involved in

1   turbulent separation bubble formation, specifically the Reynolds stress and pressure forces, as

2   previously discussed. Consequently, more frequent and intense collapses in the reattachment area

3   likely enhance the wake mode. The collapse intensity and frequency are influenced by several

4   parameters, including the bubble size, distribution, and compression rate, which are dependent on

5   *Re* and cavitation numbers.

6   Despite previous studies demonstrating the occurrence of the wake mode across various *Re*

7   numbers in single-phase flows, there remains a gap in understanding of how the Reynolds number

8   affects the shedding mode behavior. Given that the pressure and velocity fluctuations due to

9   cavitation and bubble collapses significantly impact the equilibrium between Reynolds stress and

10   pressure forces, drawing definitive conclusions about the effect of Reynolds number on the

11   shedding behavior independently is challenging.
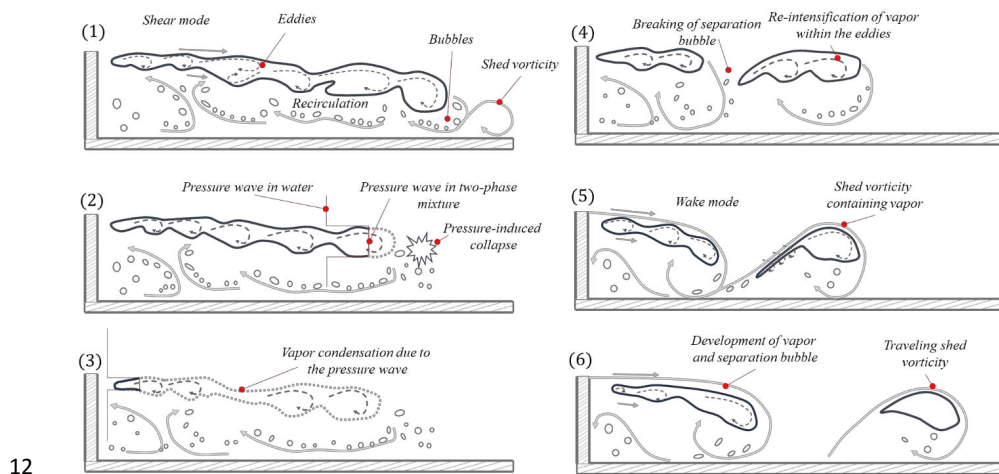
12

13   *Figure 13 Schematic illustration shear and wake mode shedding mechanism in shear cavitating flow (numbering is in accordance*

14   *with the sequence of events). (1) shear mode shedding, (2) pressure-induced collapse of vapor packet at reattachment, (3) vapor*

1   *condensation within the shear layer, (4) breaking if separation bubble, (5) wake mode shedding, and (6) development of vapor*

2   *and separation bubble.*

3

4   The frequency characteristics of Cases III and IV are examined using the pre-multiplied power

5   spectral density (PSD) at particular streamwise positions along the path of maximum fluctuation

6   in void fraction (α'_{rms}). The positions of the probes are indicated by red square zones in Figure 7

7   (right column). For Case III, the peak PSD values correspond to Strouhal numbers (St_h) of

8   approximately 0.005, 0.06, and 0.14, representing the slow, medium, and high-frequency void

9   fraction fluctuations within the shear layer (Figure 14(a)). These Strouhal numbers can be

10   interpreted as dimensionless frequencies that characterize the shedding or oscillation patterns

11   within the TSB. The dominant frequency observed at Probe 1 (plot specific to each probe is

12   determined by the probe number) for Case III falls within the medium frequency range of the PSD

13   plot. By considering the spatio-temporal map and instantaneous images in Figure 13, it can be

14   inferred that this frequency likely corresponds to the shedding of vapor packets in the wake mode

15   of the TSB. In the wake mode, almost the entire vapor content within the shear layer condenses.

16   Therefore, the observed frequency likely reflects the shedding frequency of shear cavitation in the

17   wake mode. Probes 2 and 3 exhibit a broader range of dominant frequencies, encompassing low,

18   medium, and high frequencies. The high frequencies stem from KH instabilities within the shear

19   layer, which influences the fluctuations of vapor content in this region. In the case of the micro

20   step, the flow separation and the presence of the shear layer can create velocity differences that

21   trigger the KH instability. The Kelvin-Helmholtz instability is characterized by the development

22   of spanwise vortices within the shear layer. These vortices can form due to the shearing motion

23   between the fluid layers with different velocities. As the vortices grow and interact with the

36

Physics of Fluids

AIP Publishing

1   surrounding flow, they cause mixing and deformation of the shear layer. Probe 3, situated in the

2   region of the maximum void fraction, also shows a significant presence of low-frequency

3   components in the PSD. The characteristic time scale associated with this dominant low frequency

4   is considerably larger (almost 12 times) compared to the typical frequencies of wake mode

5   shedding. This suggests that this low-frequency component is linked to external factors such as

6   pressure pump fluctuations. Finally, the dominant frequencies at Probe 4 lie in the medium and

7   high ranges, which correspond to the wake mode and shedding mode near the reattachment zone.

8   Case IV exhibits a similar pattern of dominant frequencies compared to Case III, but with two key

9   differences (Figure 14(b)). Firstly, two distinct medium frequencies are observed, particularly

10 prominent in Probes 2 and 3. These frequencies appear to be harmonics of each other, suggesting

11 a relationship between their periodicities. Secondly, the overall range of dominant frequencies in

12 Case IV is lower compared to Case III. This difference might be attributed to the influence of the

13 vapor phase on the dynamics of coherent structures within the shear layer. Similar observations

14 have been reported in other studies[20,21] .

15

1
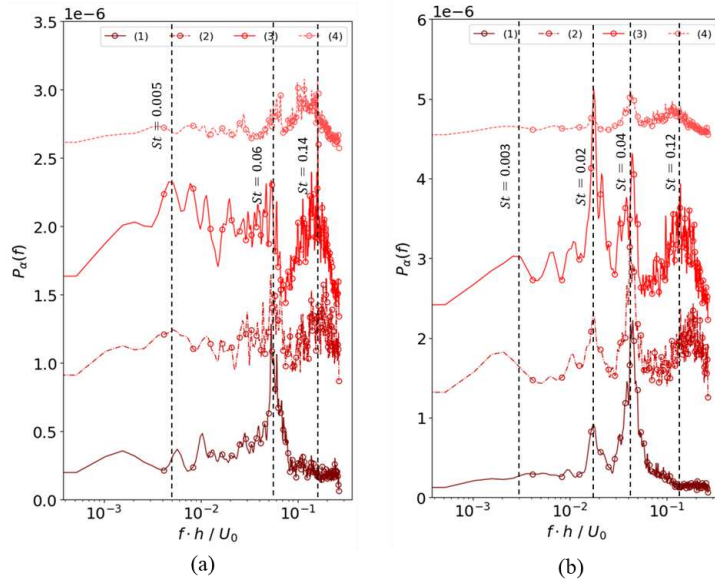
2   *Figure 14 Premultiplied power spectral density of void fraction for (a) Case III, and (b) Case IV for four probes (probes (1)-(4))*

3   *determined by red squares in Figure 8 right column (Each subplot is determined with the corresponding probe numbers 1 to 4.).*

4

5

6

7

8

9

10

11

1   **IV.   Conclusion**

2   This study presents the first comprehensive experimental investigation of shear cavitation within

3   a microscale backward-facing step (BFS) configuration. By examining four distinct cavitation

4   regimes and analyzing void fraction distribution, we identified three primary cavitation zones:

5   generation, transport, and condensation. The influence of Reynolds number and cavitation number

6   on these zones was elucidated.

7   For cases III and IV, two distinct vortex shedding mechanisms were identified near the

8   reattachment zone: wake mode and shear mode. Similar shedding regimes were documented in the

9   study by Maurice et al.[21] investigating cavitating flow within a macro-scale backward-facing

10   configuration. In our case, the wake mode was initiated by a disruption of the separation bubble.

11   This disruption resulted from the pressure wave generated by the collapse of large vapor packets,

12   which subsequently disturbed the shear layer and recirculation zone, allowing for deeper vapor

13   penetration within the channel. These findings suggest that the disturbances introduced by

14   cavitation and collapse events substantially alter the equilibrium of forces within the separation

15   bubble, ultimately triggering wake mode shedding. Conversely, the shear mode exhibits higher

16   shedding frequency with less vapor penetration. The influence of these shedding modes depends

17   on flow regimes. At higher upstream pressure (4.83 MPa), both modes are observed, with the wake

18   mode leading to deeper vapor penetration due to its stronger vortices. At lower pressure (3.79

19   MPa), weaker vortices limit vapor transport within the shear layer even during the shedding mode.

20   Additionally, the weaker vortices at lower Re number are more susceptible to pressure wave

21   condensation, which results in a more reduction in vapor content compared to the higher Re

22   number case.

1   The results indicate that nuclei predominantly accumulate in the second half of the shear layer

2   during cavitation inception, coinciding with the region of maximum void fraction. This area is also

3   where vapor bubbles collapse, generating new nuclei that become entrained within the

4   recirculation zone and contribute to subsequent cavitation. As pressure rises, nuclei distribution

5   extends throughout the separation bubble, including the first half of the shear layer and the corner

6   vortex. While the free stream is the primary source of nuclei in the inception regime, a reduction

7   in cavitation number leads to a predominance of nuclei originating from collapsing vapor packets.

8   This finding aligns with Allan et al. study[17] that incipient cavity collapse sites serve as preferential

9   locations for new bubble formation.

10   Additionally, the root mean square (RMS) of bubble concentration indicates substantial

11   fluctuations in bubble population within these regions, emphasizing the dynamic nature of the

12   nuclei distribution. Other findings, such as the association of cavitation inception with coherent

13   structures in the shear layer and the impact of cavitation on shedding dynamics, align with previous

14   studies of cavitating flow in a macroscale backward-facing step device[15,20]. These results

15   contribute significantly to understanding the influence of nuclei distribution and dynamics on

16   cavitation inception and development within microscale backward-facing step flows.

17   The results of this study offer valuable insights that may inform future research on shear cavitation

18   at the microscale. Exploring the effects of fluid properties and geometric variations on shear

19   cavitation could be a promising direction for future studies.

20

21

22

1 **Appendix A: Data Analysis**

2   In this study, the void fraction was determined by correlating the grayscale values from 2D images

3 captured by a high-speed camera with the actual void fraction, a method supported by prior

4 research [33,34]. The analysis proceeded using these grayscale values. Each frame from the high-

5 speed imaging was treated as an intensity matrix (A(t, x, y)), where (t) denotes the time index, and

6 (x) and (y) represent the row and column indices, respectively. The intensity within this matrix

7 ranges from 0 (representing black) to 255 (representing white).

8 Given that the brightness and contrast of the images remained consistent throughout the high-speed

9 capture, aligning with findings from earlier studies[33,34], we inferred that the intensity of cavitation

10 (the density of bubbles per pixel) could be proportionally estimated from the grayscale levels of

11 each image. However, it's important to note that the background also exhibits some degree of

12 greyness, potentially leading to inaccuracies in calculating the void fraction for areas deemed

13 defective. To mitigate this, we subtracted the background contribution from each snapshot matrix

14 to minimize errors.

15 Considering the significant disparity in dimensions between the depth of our device (60 µm) and

16 the width of the channel (400 µm), we anticipated minimal variation in vapor concentration along

17 the depth axis. Consequently, we disregarded these depthwise variations in our calculations.

18 Therefore, the mean and variance of void fraction can be estimated as:

19 $$\bar{\alpha}(x,y) = \frac{1}{Nt} \sum_{t=0}^{Nt} I(t,x,y)$$

20 $$var(\alpha(x,y)) = \frac{1}{Nt} \sum_{t=0}^{Nt} \left(I(t,x,y) - \bar{\alpha}(x,y) \right)^2$$

41

1 where $I(t, x, y)$ is the subtracted and normalized grey level intensity of pixel at (x, y) location

2 which belongs to the time step t. This value was obtained by subtracting the background intensity

3 and then normalizing by the maximum possible pixel value (typically 255 for 8-bit grayscale

4 images). The number of time snapshots used for data analysis was 10000 in all cases, except the

5 Case II with 1500-time snapshots.

6 The frequency characteristics of cavitation regimes (Cases III and IV) were evaluated using the

7 pre-multiplied power spectral density (PSD) at specific streamwise locations along the region of

8 maximum void fraction fluctuation (α'_{rms}) pathway. For all the cases, the sampling interval was

9 $T = 0.125\ s$ with a sampling rate of $f_s = 8e4\ Hz$. The Welch method with Hanning window was

10 utilized to compute pre-multiplied PSD for a total of 39 equal-length segments in time with 50%

11 overlap[35,36]. Each segment comprised 512 samples, and the resulting frequency range was $St_h =$

12 $\frac{fH}{U_0} = 4e - 4{\sim}0.2$.

13 A method similar to Allan et al. [17], was employed to quantify bubble nuclei from high-speed

14 camera images. First, the background subtraction and normalization were performed on the

15 grayscale images. This process removed background noise and ensured consistency across images.

16 For each cavitation regime, a 3D matrix was created, with two spatial dimensions representing

17 bubble location and a third dimension representing time. A threshold intensity value (10% of

18 maximum pixel intensity) was used to identify potential void regions (areas with vapor bubbles)

19 within each pixel. The matrix was then segmented into void and non-void regions. Void regions

20 were subdivided into disconnected groups (groups without shared pixels). Subsequently, in each

21 time frame, connected groups smaller than a threshold size (25 µm in each direction) were

22 considered as potential nuclei. Notably, a single group within the 3D matrix could track the

movement and evolution of a single bubble over time. Finally, the spatial 2D domain was discretized into subdomains with a size of $100\mu m \times 100\mu m$. The average RMS of the number of nuclei within each subdomain were calculated. This approach could provide information about both the average and fluctuating characteristics of the nuclei distribution.

ACKNOWLEDGMENTS

DATA AVAILABILITY

The data that support the findings of this study are available from the corresponding authors upon reasonable request.

References

[1] C.E. Brennen, *Cavitation and Bubble Dynamics* (Cambridge University Press, Cambridge, 2013).

[2] M. Ghorbani, A.K. Sadaghiani, L.G. Villanueva, and A. Koşar, "Hydrodynamic cavitation in microfluidic devices with roughened surfaces," Journal of Micromechanics and Microengineering **28**(7), (2018).

[3] F. Rokhsar Talabazar, A. Sheibani Aghdam, M. Jafarpour, D. Grishenkov, A. Koşar, and M. Ghorbani, "Chemical effects in 'hydrodynamic cavitation on a chip': The role of cavitating flow patterns," Chemical Engineering Journal **445**, 136734 (2022).

[4] F. Rokhsar Talabazar, M. Maleki, A. Sheibani Aghdam, D. Grishenkov, M. Ghorbani, and A. Koşar, "Cavitation inception and evolution in cavitation on a chip devices at low upstream pressures," Physics of Fluids **35**(1), 012012 (2023).

[5] M. Ghorbani, A. Mohammadi, A.R. Motezakker, L.G. Villanueva, Y. Leblebici, and A. Koşar, "Energy Harvesting in Microscale with Cavitating Flows," ACS Omega **2**(10), 6870–6877 (2017).

[6] S. Seyedmirzaei Sarraf, F. Rokhsar Talabazar, I. Namli, M. Maleki, A. Sheibani Aghdam, G. Gharib, D. Grishenkov, M. Ghorbani, and A. Koşar, "Fundamentals, biomedical applications and future potential of micro-scale cavitation-a review," Lab Chip **22**(12), 2237–2258 (2022).

[7] M. Jafarpour, A.S. Aghdam, M.T. Gevari, A. Koşar, M.K. Bayazıt, and M. Ghorbani, "An ecologically friendly process for graphene exfoliation based on the 'hydrodynamic cavitation on a chip' concept," RSC Adv. **11**(29), 17965–17975 (2021).

[8] F. Rokhsar Talabazar, M. Jafarpour, M. Zuvin, H. Chen, M.T. Gevari, L.G. Villanueva, D. Grishenkov, A. Koşar, and M. Ghorbani, "Design and fabrication of a vigorous 'cavitation-on-a-chip' device with a multiple microchannel configuration," Microsyst Nanoeng **7**(1), 44 (2021).

[9] M. Ghorbani, A.S. Aghdam, M.T. Gevari, A. Koşar, F.Ç. Cebeci, D. Grishenkov, and A.J. Svagan, "Facile hydrodynamic cavitation ON CHIP via cellulose nanofibers stabilized perfluorodroplets inside layer-by-layer assembled SLIPS surfaces," Chemical Engineering Journal **382**, 122809 (2020).

[10] J.-J.(于佳佳) Yu, L.-Y.(蒋璐阳) Jiang, L.(黄利) Huang, G.-Y.(李谷元) Li, M. Bake, and Y.-R.(李友荣) Li, "Hydrodynamic cavitation of nematic liquid crystal in Stokes flow behind bluff body with different shapes in microchannel," Physics of Fluids **36**(1), 012006 (2024).

1 [11] M. Ghorbani, M. Yildiz, D. Gozuacik, and A. Kosar, "Cavitating nozzle flows in micro- and
2 minichannels under the effect of turbulence," Journal of Mechanical Science and Technology
3 **30**(6), 2565–2581 (2016).

4 [12] D. Podbevšek, M. Petkovšek, C.D. Ohl, and M. Dular, "Kelvin-Helmholtz instability governs the
5 cavitation cloud shedding in Venturi microchannel," International Journal of Multiphase Flow
6 **142**, 103700 (2021).

7 [13] R.E.A. Arndt, "CAVITATION IN VORTICAL FLOWS," Annu Rev Fluid Mech **34**(1), 143–175 (2002).

8 [14] K. Agarwal, O. Ram, and J. Katz, "Cavitating Structures at Inception in Turbulent Shear Flow,"
9 in *Proceedings of the 10th International Symposium on Cavitation (CAV2018)*, edited by J. Katz,
10 (ASME Press, 2018), p. 0.

11 [15] K. Agarwal, O. Ram, Y. Lu, and J. Katz, "On the pressure field, nuclei dynamics and their
12 relation to cavitation inception in a turbulent shear layer," J Fluid Mech **966**, A31 (2023).

13 [16] V. Aeschlimann, S. Barre, and H. Djeridi, "Velocity field analysis in an experimental cavitating
14 mixing layer," Physics of Fluids **23**(5), 055105 (2011).

15 [17] E.S.C. Allan, L. Barbaca, J.A. Venning, P.S. Russell, B.W. Pearce, and P.A. Brandner, "Nucleation
16 and cavitation inception in high Reynolds number shear layers," Physics of Fluids **35**(1), 013317
17 (2023).

18 [18] F.L. Brandao, M. Bhatt, and K. Mahesh, "Numerical study of cavitation regimes in flow over a
19 circular cylinder," J Fluid Mech **885**, A19 (2020).

20 [19] A. Gnanaskandan, and K. Mahesh, "Large Eddy Simulation of the transition from sheet to
21 cloud cavitation over a wedge," International Journal of Multiphase Flow **83**, 86–102 (2016).

22 [20] A. Bhatt, H. Ganesh, and S.L. Ceccio, "Cavitating flow behind a backward facing step,"
23 International Journal of Multiphase Flow **139**, 103584 (2021).

24 [21] G. Maurice, N. Machicoane, S. Barre, and H. Djeridi, "Coupled x-ray high-speed imaging and
25 pressure measurements in a cavitating backward facing step flow," Phys Rev Fluids **6**(4), 44311
26 (2021).

27 [22] X. Lv, W.-T. Wu, J. Lv, K. Mao, L. Gao, and Y. Li, "Study on the Law of Pseudo-Cavitation on
28 Superhydrophobic Surface in Turbulent Flow Field of Backward-Facing Step," Fluids **6**(6), (2021).

29 [23] M. Maleki, F. Rokhsar Talabazar, A. Koşar, and M. Ghorbani, "On the spatio-temporal dynamics
30 of cavitating turbulent shear flow over a microscale backward-facing step: A numerical study,"
31 International Journal of Multiphase Flow **177**, 104875 (2024).

1 [24] S.J. Kline, "Describing Uncertainties in Single-Sample Experiments," Mechanical Engineering
2 **75**, 3–8 (1953).

3 [25] J. Katz, and T.J. O'Hern, "Cavitation in Large Scale Shear Flows," J Fluids Eng **108**(3), 373–376
4 (1986).

5 [26] G. Maurice, H. Djeridi, and S. Barre, "Experimental investigation of a cavitating backward-
6 facing step flow," IOP Conf Ser Earth Environ Sci **22**(5), 052008 (2014).

7 [27] P.E. Dimotakis, "Two-dimensional shear-layer entrainment," AIAA Journal **24**(11), 1791–1796
8 (1986).

9 [28] F. Durst, and C. Tropea, "Flows over Two-Dimensional Backward — Facing Steps," in *Structure*
10 *of Complex Turbulent Shear Flow*, edited by R. Dumas and L. Fulachier, (Springer Berlin
11 Heidelberg, Berlin, Heidelberg, 1983), pp. 41–52.

12 [29] F. SCHÄFER, M. BREUER, and F. DURST, "The dynamics of the transitional flow over a
13 backward-facing step," J Fluid Mech **623**, 85–119 (2009).

14 [30] P.M. Nadge, and R.N. Govardhan, "High Reynolds number flow over a backward-facing step:
15 structure of the mean separation bubble," Exp Fluids **55**(1), 1657 (2014).

16 [31] L.M. Hudy, A. Naguib, and W.M. Humphreys, "Stochastic estimation of a separated-flow field
17 using wall-pressure-array measurements," Physics of Fluids **19**(2), 024103 (2007).

18 [32] M. Ji, and M. Wang, "Surface pressure fluctuations on steps immersed in turbulent boundary
19 layers," J Fluid Mech **712**, 471–504 (2012).

20 [33] I. Bilu, G. Bombek, B. irok, M. Hoevar, T. Cencîc, and M. Petkovek, "The experimental analysis
21 of cavitating structure fluctuations and pressure pulsations in the cavitation station," Strojniski
22 Vestnik-Journal of Mechanical Engineering **60**, 147–157 (2014).

23 [34] C. Wang, and M. Zhang, "Dynamics of cavity structures and wall-pressure fluctuations
24 associated with shedding mechanism in unsteady sheet/cloud cavitating flows," Flow **3**, E9
25 (2023).

26 [35] Y. NA, and P. MOIN, "Direct numerical simulation of a separated turbulent boundary layer," J
27 Fluid Mech **374**, 379–405 (1998).

28 [36] W. Hu, S. Hickel, and B. van Oudheusden, "Dynamics of a supersonic transitional flow over a
29 backward-facing step," Phys Rev Fluids **4**(10), 103904 (2019).

30

1

2

3

4

5

6

7

8

9